Regimes in Wet Wollastonite Carbonation: A Comparative Kinetics and Multi-Technique Investigation

Sahra Homaee[123], Robert Möckel[1], Doreen Ebert[1], Martin Rudolph[1]

Abstract

Calcium silicate minerals, including wollastonite, are considered promising feedstocks for mineral carbonation, particularly for applications in low-carbon building and construction materials; however, the mechanisms governing their behavior under near-ambient wet conditions are not yet fully understood. This study examines the mechanistic influence of specific operational parameters on wollastonite wet carbonation under additive-free, near-ambient conditions. Two representative carbonated samples, exhibiting low (approximately 6 %) and high (approximately 50 %) carbonation efficiencies, were selected from a systematic screening for detailed analysis. These samples exemplify contrasting regimes of gas-liquid and solid-liquid mass transfer, primarily influenced by CO_2 flow rate and agitation speed. An integrated characterization strategy, incorporating XRF, TGA, XRD, BET, Pycnometry, and SEM-EDX, along with time-resolved kinetic model fitting, was employed. Phase and microstructural analyses reveal limited carbonate formation and sparse, discontinuous precipitates under mass-transfer-limited conditions, whereas extensive calcite precipitation and coalescing intergranular carbonate domains develop when mass transfer is enhanced. Variations in specific surface area, skeletal density, and thermal decomposition behavior correspond to progressive carbonate maturation during the reaction. Kinetic analysis of independent batch experiments at varying carbonation times indicates that both the Avrami model and the surface-reaction-controlled shrinking-core model accurately describe the reaction from the initial stages and remain applicable throughout the process. At extended reaction times, the diffusion-controlled shrinking-core model fits the data, reflecting the increasing significance of diffusional resistance as a carbonate-silica product layer forms.

[1]Helmholtz-Zentrum Dresden-Rossendorf, Helmholtz Institute Freiberg for Resource Technology, Freiberg, Germany

[2] Technische Universität Dresden (TU Dresden), Dresden, Germany

[3] HZDR Innovation GmbH, Helmholtz-Zentrum Dresden-Rossendorf (HZDR), Dresden, Germany

These findings provide a coherent mechanistic framework that links operational conditions to the evolution of reaction pathways during wollastonite wet carbonation under near-ambient conditions.

Key words: Wollastonite, near-ambient wet carbonation; calcite, kinetics, CCU, CCSU

1 Introduction

Mitigating anthropogenic CO_2 emissions remains a key challenge for industry and research. Technological strategies for mitigation generally encompass two main approaches: reducing CO_2 generation through methods such as fuel switching and efficiency improvements, and managing emitted CO_2 through carbon capture, utilization, and storage (CCUS) or carbon dioxide removal, with efforts concentrated on practical, affordable solutions especially in areas where CO_2 emission stems from other sources than fuel as in the case of cement production. Within CCUS, mineral carbonation offers a durable method for fixing CO_2 by transforming Ca/Mg-bearing minerals or wastes (oxides, hydroxides, silicates) into thermodynamically stable carbonates, which can yield valuable byproducts [1,2].

A wide variety of feedstocks is suitable, including natural silicates (e.g., olivine, serpentine, wollastonite), mining residues, and industrial by-products (e.g., steel slag, cement fines). The choice of feedstock should match the intended end use (e.g., supplementary cementitious materials (SCMs), aggregates) to ensure proper performance and reduce downstream risks [1,3–5].

The cement industry, one of the largest sources of anthropogenic CO_2 emissions, presents a particularly relevant application for mineral carbonation. Reducing emissions from the construction sector is critical to limiting global warming to below 1.5°C by the end of this century. The cement industry alone accounts for approximately 7 % of global CO_2 emissions [6,7]. In 2019, the broader construction sector emitted about 9.95 Gt CO_2, making it the highest contributor to industrial emissions. Projections suggest a 16 % reduction by 2030, with a net-zero target by 2050 [8]. Incorporating mineral carbonation into cement production could create a closed-loop process where captured CO_2 is mineralized and reused within the same supply chain, potentially leading to carbon-negative cement as standards and incentives develop [1,6].

Within ex-situ mineral carbonation, both direct (additive-free) and indirect routes are employed, and the processes can be wet, dry, or semi-dry, depending on the feedstock and reactor design.

Although Ca/Mg silicates offer permanent storage, reaction kinetics are often slow under mild, direct conditions, and mechanism-rate relationships remain insufficiently understood [1,9,10].

Selecting the most reactive mineral is therefore essential for advancing mineral carbonation research. Of the two main categories of silicate minerals, calcium silicates are more reactive. Among calcium silicate minerals, wollastonite ($CaSiO_3$) is recognized as one of the most reactive options in direct ex-situ wet carbonation systems [1,11]. This higher reactivity of wollastonite makes it particularly suitable for kinetic modeling and online process monitoring via spectroscopic methods, such as Raman spectroscopy, as it enables more precise observation of reaction pathways and opportunities for improvement. By beginning with the most reactive minerals, researchers can better model the kinetics, offering insights that could be integral to optimizing carbonation processes and enhancing scalability. In the next step, these basics can be applied to more complex systems, such as tailings [12,13].

The primary process occurs in two main steps: (1) leaching of Ca^{2+} from the wollastonite matrix into solution, and (2) nucleation and growth of $CaCO_3$ (calcium Carbonate) from the dissolved calcium and carbonate ions [12,14,15]. Then, paying attention to these two main steps (1 and 3) is crucial to studying this reaction.

1. *Leaching:

   $CaSiO_3\,(s) + 2H^+\,(aq) \rightarrow Ca^{2+}\,(aq) + H_2O\,(l) + SiO_2\,(s)$

2. CO_2 dissolution and (bi)carbonate species conversion.

   $CO_2\,(g) + H_2O\,(l) \leftrightarrow H_2CO_3\,(aq) \leftrightarrow HCO_3^-\,(aq) + H^+\,(aq)$

3. *Nucleation and growth:

   $Ca^{2+}\,(aq) + HCO_3^-\,(aq) \rightarrow CaCO_3\,(s) + H^+\,(aq)$

From a mechanistic perspective, previous studies indicate that the silica-rich rim initially forms via interfacial dissolution and precipitation. In purely aqueous systems, the rim does not significantly hinder Ca^{2+} release, so reaction kinetics are predominantly governed by surface reactions. In contrast, in alkaline, saline, or supercritical CO_2 systems, the precipitation of additional carbonate or silicate phases can densify the rim and partially block it, shifting the overall kinetics toward

diffusion control through the product layer. This transition is strongly influenced by system chemistry, water availability, and secondary phase formation characteristics [12,16,17]. Importantly, these coupled steps show why there is no universal "recipe" for speeding up wollastonite carbonation. Increasing the dissolution rate, whether by raising temperature or lowering pH to boost hydronium activity, indeed boosts Ca^{2+} release, but at the same time decreases dissolved carbonate availability because of lower CO_2 solubility at higher temperature or reduced carbonate speciation at lower pH. As a result, conditions that encourage Ca^{2+} leaching may suppress carbonate availability, and vice versa. This interplay emphasizes that the limiting steps can differ across studies and operating conditions. Therefore, systematically investigating various parameters and reaction environments is essential to identifying the dominant rate-limiting mechanism and developing optimized, process-specific carbonation strategies.

Although numerous studies investigate the influence of operating variables such as temperature, solid-to-liquid ratio, CO_2 delivery or pressure, and mixing on overall conversion, relatively few address how these factors alter the rate-controlling step or impact microstructural evolution [15,16].

Previous studies have examined wollastonite carbonation within a limited range of practical operating conditions, and most research focuses on elevated temperatures, pressure, or the use of additives (solution chemistry) to speed up the reaction. High temperature and pressure help speed up this process, similar to how various additives like acids (formic, acetic) and sodium bicarbonate are used [5,18–22]. All these factors that accelerate the process interfere with the actual and direct wollastonite wet carbonation, making it essential to first investigate this step to fully understand the main controlling parameters. With this foundational understanding, scientists can then develop better conditions to enhance the process. This study aims to address this need. Specifically, the objectives of this research are to thoroughly investigate the main parameters controlling the wollastonite wet carbonation process under near-ambient conditions and to establish a comprehensive understanding of these factors to optimize the reaction for practical applications.

This experimental study begins with an initial screening phase to define practical operating ranges and choose two conditions for a detailed study, giving a clear basis for the samples used. Research on near-ambient, additive-free wet carbonation of wollastonite is still limited, and studies that focus on the reaction mechanism under these mild conditions are rare. To fill this gap, we use several characterization methods (X-ray Fluorescence (XRF), Thermogravimetric Analysis (TGA), X-ray

Diffraction (XRD), Brunauer–Emmett–Teller (BET), and Scanning Electron Microscopy (SEM)) and test different linearized kinetic models. We include models like the Avrami framework and the shrinking-core (surface-reaction and diffusion–controlled) approach because they are well-suited to describe Ca-leaching and the formation of carbonate product layers during Ca-silicate carbonation.

We chose these characterization methods because they each offer different insights into the microstructural changes that drive the reaction. As mentioned earlier, aqueous wollastonite carbonation has two main rate-controlling steps: first, Ca^{2+} leaches from the silicate structure, and second, the calcium carbonate product layer forms and grows. XRF, TGA and XRD help identify the elements, and phases in both intermediate and final products, while BET and SEM shows changes in surface area and shape, which are important for understanding how the material dissolves and how the product layer develops. By combining these analytical and kinetic approaches, we can connect microstructural changes to reaction mechanisms and develop useful guidelines for using CO_2 in cement processes.

2 Materials and Methods

The main material used in this study is natural wollastonite (Töpfereibedarf Lehrer GesmbH, Austria). XRF analysis indicated that the sample matched typical wollastonite compositions. The raw material was used as received, without further purification. Prior to carbonation experiments, the feedstock was characterized to establish its baseline chemical, mineralogical, and physical properties. More details are in the section 3.1.

2.1 Analytical Instruments and Purposes

Several analytical techniques were used to characterize the chemical, structural, and physical properties of wollastonite before and after carbonation. Elemental composition was determined by wavelength-dispersive X-ray fluorescence analysis (WD-XRF) using a PANalytical AxiosmAX spectrometer equipped with an Rh anode, operated with SuperQ5 software. Samples were analyzed as fused glass beads following the calibrated wide-range oxide program (Wroxi; 25 kV-60 kV, 66 mA-160 mA). Prior to fusion, powders were ground to <63 µm using a Retsch disc mill (tungsten carbide pot). Samples were dried overnight at 105°C, then annealed for 2 h at 950 °C to determine loss on ignition (LOI). For bead preparation, 1.125 g of annealed sample was mixed with 9.0 g

$Li_2B_4O_7$ flux (≈1:8) in a Pt crucible and fused at 1050°C using a Claisse TheOx Advanced melting furnace. Crystalline phases were identified by powder XRD using a PANalytical Empyrean diffractometer with a Co X-ray tube (35 kV, 35 mA), Fe Kβ-filter, and a PIXcel3D (Medipix3 1×1) area detector. Patterns were collected from 5°- 80° (2θ) with a step size of 0.0131° (irradiated area 15 mm×12 mm, total acquisition time 153 min). Qualitative phase identification was performed in PANalytical HighScore (3.0.4) using the ICDD PDF-5+ (2025) database. Quantitative phase analysis was obtained by Rietveld refinement using Profex(5.1.0) [23]. The data obtained from Rietveld refinement are perfectly consistent with results from other techniques, such as XRF. However, these results require careful evaluation because standard micronization, typically performed using a Retsch McCrone mill, was not feasible due to the potential alteration of the carbonated samples. Consequently, additional sample treatment was minimized.

Thermogravimetric analysis (TGA) was used to quantify the natural CO_2 content and to determine the total CO_2 uptake following carbonation. Measurements were performed using a NETZSCH TG 309 Libra Classic under a nitrogen atmosphere, with a heating rate of 20 $K \cdot min^{-1}$ from 30°C to 1000°C. Particle size distribution was evaluated with laser diffraction (Sympatec HELOS, Germany). Surface properties were assessed through Brunauer–Emmett–Teller (BET) nitrogen adsorption to determine the specific surface area (SSA) using a Micromeritics Gemini VII 2390t analyzer (Gemini VII software 5.00), following DIN ISO 9277:2022. Prior to analysis, samples were degassed at 200°C for 3 h under flowing nitrogen gas; measurements were performed with nitrogen gas as the adsorptive gas using an equilibration time of 5 s, and Skeletal density was measured by helium gas pycnometry using an AccuPyc II 1340 pycnometer (V2.01; serial no. 3356), following DIN 66137-2. Measurements were performed with helium gas as the analysis gas, using an equilibrium rate of 0.005 $psig \cdot min^{-1}$ and 20 purge cycles prior to analysis (sample mass ~11.72 g; chamber insert 35 cm^3; cell volume 39.6119 cm^3). Microstructural features, including particle morphology, dissolution textures, and carbonate precipitation, were examined by scanning electron microscopy (SEM). Samples were carbon-coated using a Leica EM MED020 carbon coater prior to analysis. SEM and energy-dispersive X-ray spectroscopy (EDX) analyses were performed using a FEI Quanta 650 FEG field-emission gun scanning electron microscope equipped with two Bruker Quantax X-Flash 5030 energy dispersive X-ray spectrometers (EDX). The instrument was operated at an accelerating voltage of 15 kV, and a working distance of approximately 13 mm. Elemental maps were acquired using Bruker Esprit software.

These techniques collectively enable the evaluation of compositional changes, phase evolution, surface modification, and morphological development associated with the carbonation process.

2.2 Experimental Setup and Procedure

This section explains the study's methodology, covering the investigation of wet carbonation reaction mechanisms under specific conditions. It details the main experimental design, sample selection strategy, the kinetic study procedure, and the determination of theoretical CO_2 uptake.

2.2.1 Main Experimental Design for Carbonation and Samples Selection

The experiments were conducted at atmospheric pressure using a reflux setup/ Batch reactor, which include a three-necked reactor fitted with a condenser, thermometer, and magnetic stirrer-heater. A pressurized CO_2 cylinder provided the pure CO_2 source, with flow rate regulated by a flowmeter (Figure 1).

Before carbonation, wollastonite was ground using a disc mill (Retsch RS 200, Germany) for 10 min. After the system reached the target temperature and the CO_2 flow was stabilized, the wollastonite was added according to the specified solid-to-liquid ratio (S/L) (Table 1). The reaction time was fixed at 2 hours. Following carbonation, the slurry was dried at 105°C for 12 hours before further analysis.

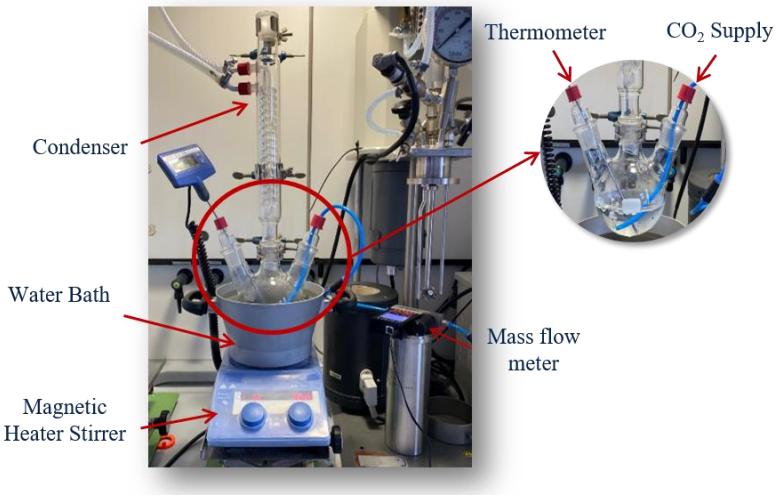

Figure 1 Reflux Setup

2.2.2 Sample Selection

A structured design-of-experiments (DOE) screening was conducted to map the near-ambient wet carbonation space for Wollastonite, considering factors such as solid-to-liquid ratio (S/L), temperature (T), agitation speed (rpm), and CO_2 flow rate. Based on DOE responses, specifically normalized CO_2 uptake obtained from thermogravimetric analysis (TGA), two representative conditions were selected for the mechanistic study: i.e. the highest carbonated (optimum) and the lowest carbonated conditions. These selected conditions were subsequently rerun for use in this study. The selected samples and their operating conditions are summarized in Table 1. The least carbonated sample is compared with other samples that vary in solid-to-liquid ratio, rotational speed, and CO_2 flow rate. As phase changes are the primary indicator for monitoring mineral carbonation, Table 2 provides a quantitative representation of all potential carbonatable phases and their transformations under these conditions.

Table 1 selected conditions and obtained the CO_2 uptake from each

Selected samples' Operation conditions					
Run	*T* (°C)	*S/l* (%)	*CO_2.flow* (mL/min)	*rpm* (min^{-1})	*CO_2Uptake* (%)
Lowest	90	30	100	300	1.97
Highest	90	10	700	900	15.29

2.2.3 **Kinetics experiments protocol**

The kinetics study employed the optimal condition identified in the previous Design of Experiments (DOE) screening, specifically the condition yielding the highest carbonation degree. The wet carbonation process was replicated under identical operating conditions with varying reaction times. Based on the DOE, which indicated an optimum at approximately 120 minutes, a non-uniform time schedule was implemented (0, 5, 10, 15, 20, 30, 45, 60, 75, 90, 120, 150, and 180) min to elucidate early-time kinetics, incorporate the 120-minute optimum, and verify the plateau or passivation phase. To maintain consistent solid-liquid ratios, hydrodynamic conditions, and gas–liquid interactions, separate batch experiments were conducted for each time point and the reaction was stopped at the predetermined endpoint, totaling 12 runs. This approach prevented artifacts such as volume loss, sediment-liquid drift, CO_2 depletion, or temperature disturbances.

All final products were dried for 12 hours at 105°C, with phase changes assessed by XRD and CO_2 uptake measured by TGA.

To identify the most suitable kinetic model, the integral (linearized) fitting approach was employed. The linear forms of candidate models were plotted against time, parameters were obtained by linear regression, and model suitability was evaluated based on the R^2 value.

2.3 Determination of theoretical CO_2 Uptake

CO_2 uptake (theoretical and experimental).

Theoretical CO_2 uptake was estimated from bulk chemistry using XRF, under the assumption that only CaO and MgO undergo carbonation as described in the following reactions (1,2).

$$CaO(s) + CO_2(g) \rightarrow CaCO_3(s) \quad (1)$$

$$MgO(s) + CO_2(g) \rightarrow MgCO_3(s) \quad (2)$$

For a 1 g sample with X % (*m*/*m*) CaO and Y % (*m*/*m*) MgO, the potential CO_2 gain is calculated as follows

$$X\,\%\ (m/m)\ \mathrm{CaO} \times \frac{1\ \mathrm{mol\ CaO}}{56.07\ \mathrm{g\ CaO}} \times \frac{1\ \mathrm{mol\ CO_2}}{1\ \mathrm{mol\ CaO}} \times \frac{44\ \mathrm{g\ CO_2}}{1\ \mathrm{mol\ CO_2}} = X\,\% \times 0.78\ \mathrm{CO_2} \quad (3)$$

$$Y\,\%\ \mathrm{MgO} \times \frac{1\ \mathrm{mol\ MgO}}{40.3\ \mathrm{g\ MgO}} \times \frac{1\ \mathrm{mol\ CO_2}}{1\ \mathrm{mol\ MgO}} \times \frac{44\ \mathrm{g\ CO_2}}{1\ \mathrm{mol\ CO2_2}} = Y\,\% \times 1.1\ \mathrm{CO_2} \quad (4)$$

$$CO_2^{theoretical}(g) = 0.78\,X + 1.1\,Y \quad (5)$$

For comparison as mass percent, this value was corrected to account for native carbonate content as measured by thermogravimetric analysis (TGA)

$$\text{Theoretical } CO_2 \text{ Uptake (\%)} = (0.78 \cdot X + 1.1 \cdot Y) * 100\ \% - \text{Natural } CO_2\ (\%) \quad (6)$$

Therefore, based on the XRF and natural CO_2 uptake measured by TGA, after this calculation, since the CaO and MgO in the wollastonite sample reported as X = 42.9 %(*m*/*m*) and

Y = 1.6 %(*m*/*m*) (XRF based) and Natural CO_2 was 3.34 % (TGA based), the theoretical CO_2 uptake is 31.8 %.

Theoretical CO_2 Uptake % = (0.78·(42.9 %) + 1.1(1.6 %)) – 3.34 % = 31.8 % (6-a)

Experimental CO_2Uptake quantified the net amount of CO_2 sequestered in the solid as a result of carbonation. To isolate CO_2 fixed during the reaction, the CO_2 content originally present in the feed material was subtracted from that measured in the carbonated sample.

Thermogravimetric analysis (TGA) determined CO_2 content by measuring mass loss associated with carbonate decomposition in the 500°C–900°C temperature range. This interval was chosen because it predominantly corresponds to CO_2 release from carbonate phases. To compare samples with varying total mass losses, the carbonate-related mass loss was normalized by the total mass loss measured between 30°C and 975°C, representing the effective solid mass after removal of moisture.

Accordingly, CO_2 uptake was calculated as the difference between the normalized carbonate mass loss of the carbonated sample and that of the feed, with the result rescaled to the initial sample mass. This procedure ensures that the reported CO_2 uptake reflects only the net CO_2 sequestered by carbonation, excluding contributions from pre-existing carbonates in the feed material.

The final normalized CO_2 uptake is calculated as the difference between the Feed and carbonated sample states (this method was used and described before in [24]):

$$CO_2\ \text{Uptake}\ \% = \left(\frac{\Delta m_{Carb,500-900}}{100-\Delta m_{Carb,30-975}} - \frac{\Delta m_{Feed,500-900}}{100-\Delta m_{Feed,30-975}}\right) \times \frac{100-\Delta m_{Carb,30-975}}{100} \quad (7)$$

$$\Delta m_{x,500\text{-}900} = m_{x,500°C} - m_{x,900°C} \quad (7\text{-a})$$

$$\Delta m_{x,30\text{-}975} = m_{x,30°C} - m_{x,975°C} \quad (7\text{-b})$$

Where x denotes the sample state, with x = Carb for the carbonated sample and x = Feed for the uncarbonated material, $\Delta m_{x,500-900}$ represents the mass loss associated with carbonate decomposition (CO_2 release) and $\Delta m_{x,30-975}$ corresponds to the total mass loss used for normalization.

3 Results and discussion

3.1 Characterization of the Feedstock (Raw Wollastonite)

The raw wollastonite was characterized to establish baseline chemical, mineralogical, and physical properties prior to carbonation. XRF analysis confirmed a Ca–Si composition typical of wollastonite, with key oxide components as listed in Table 3. XRD analysis verified wollastonite as the dominant crystalline phase, accompanied by minor phases such as Calcite (c.f.Table 2). The particle size distribution obtained by laser diffraction resulted in the size weight balanced quantiles (10 %, 50 % and 90 %) and Sauter mean diameter (ST) as in Table 4. BET measurements provided an initial specific surface area of 4.67 $m^2 \cdot g^{-1}$, while gas pycnometry determined the skeletal density to be 2.895 $g.cm^{-3}$ (c.f. Table 5). SEM imaging revealed elongated, bladed particles typical of wollastonite, serving as a microstructural reference for comparison with selected carbonated samples (c.f. Figure 3).

Table 2 Mineralogical composition of the feed sample, determined by Quantitative X-ray diffraction (QXRD)

Phase	Chemical Formula	Weight %
Wollastonite	$CaSiO_3$	75.5
Calcite	$CaCO_3$	8.3
Quartz	SiO_2	8.4
Pyroxene	$CaMgSi_2O_6$	7.9

Table 3 Chemical composition of the feed sample (XRF)

Oxide	SiO_2	CaO	TiO_2	Al_2O_3	Fe_2O_3	Mn_3O_4	MgO	K_2O
Weight %	51.76	42.91	0.02	0.27	0.38	0.05	1.6	0.03

Table 4 PSD of Raw wollastonite

Parameter	Value
$d_{10,3}$	0.8 μm
$d_{50,3}$	4.2 μm

$d_{90,3}$	24.0 μm
d_{ST}	2.2 μm

3.2 Carbonation degree and phase identification

Quantitative X-Ray Diffraction (QXRD) was employed to compare the phase assemblage of the feed with two selected carbonated samples representing the lowest and highest CO_2 uptake (Figure 2). The feed is dominated by wollastonite (75.5 % (*m*/*m*)), with minor amounts of calcite (8.3 % (*m*/*m*)), quartz (8.4 % (*m*/*m*)), and pyroxene (7.9 % (*m*/*m*)). After carbonation, the relative wollastonite content decreases while calcite increases, confirming that $CaCO_3$ is the main reaction product and that the degree of carbonation differs between the two selected conditions.

In the lowest-uptake sample, wollastonite remains the major phase (67.8 % (*m*/*m*)), while calcite increases moderately to 13.2 % (*m*/*m*), indicating limited conversion. In contrast, the highest-uptake sample exhibits a pronounced increase in calcite (49.8 % (*m*/*m*)) and a substantial decrease in wollastonite (33.8 % (*m*/*m*)), consistent with a significantly higher conversion. The contents of quartz and pyroxene remain comparatively low (approximately 7.8 % (*m*/*m*) – 8.6 % (*m*/*m*)) and do not follow the same trend as wollastonite and calcite, suggesting that these phases are largely inert under the applied carbonation conditions and primarily reflect the mineralogical background of the feed.

Also, this phase analysis of selected samples shows a clear increase in apparent calcite crystallite size, progressing from the feed to the low-uptake product and then to the high-uptake product. This trend suggests progressive calcite crystallite growth and improved crystallinity as carbonation advances and conversion increases. The feed sample exhibits the smallest apparent crystallite size, while both carbonated samples display substantially larger values. The high-uptake sample contains the largest crystallites, which is consistent with more sustained nucleation and growth under favorable mass-transfer conditions. In addition, the apparent calcite crystallite size increases from the low-uptake to the high-uptake sample, indicating more developed carbonate domains under high-uptake operating conditions. This trend aligns with the distinct process parameters of the high-uptake regime, characterized by higher RPM, increased CO_2 flow rate, and a lower solid-to-liquid (S/L) ratio enhancing hydrodynamics and CO_2 availability, thereby supporting sustained precipitation and crystallite growth. In contrast, the low-uptake regime, with lower RPM, reduced

CO_2 flow rate, and a higher S/L ratio, is more limited by transport and encourages localized precipitation with restricted growth. This evolution in crystallite size is consistent with the trends observed in the BET and TGA/DTG datasets, which are examined in detail in subsequent sections.

The kinetics study shows a clear, time-dependent trend in both phase assemblage and carbonate development as a function of carbonation duration. QXRD analysis reveals a gradual increase in calcite content with reaction time, accompanied by a corresponding decrease in the wollastonite phase, confirming ongoing conversion via calcium dissolution and $CaCO_3$ precipitation. In contrast, the other phases, such as quartz and pyroxene, remain nearly constant throughout the experiment, indicating that the primary changes result from wollastonite consumption and carbonate formation rather than the transformation of minor silicate phases. Additionally, the apparent calcite crystallite size, as determined by XRD peak broadening, increases from approximately 90 nm at early reaction times to 150 nm – 160 nm at 180 min, reflecting progressive crystal growth and improved crystallinity of the carbonate product as carbonation advances. It is important to note that the reported crystallite size values are provided for comparative purposes only, as the powders were not micronized prior to XRD analysis, and particle-size heterogeneity or preferred orientation may affect peak profiles and impact the true crystallite size values. However, consistent application of the fitting protocol across the entire time series supports the conclusion that extended carbonation duration enhances both calcite yield and the formation of larger, more stable calcite crystallites. The consistent increase in crystallite size supports a time- and conversion-dependent development of more stable calcite domains. These kinds of observations, such as increasing calcite crystallite size over time and during carbonation, influenced by parameters like increased CO_2 flow rate and temperature, have been reported in some studies to contribute to cement and building materials carbonation [25,26].

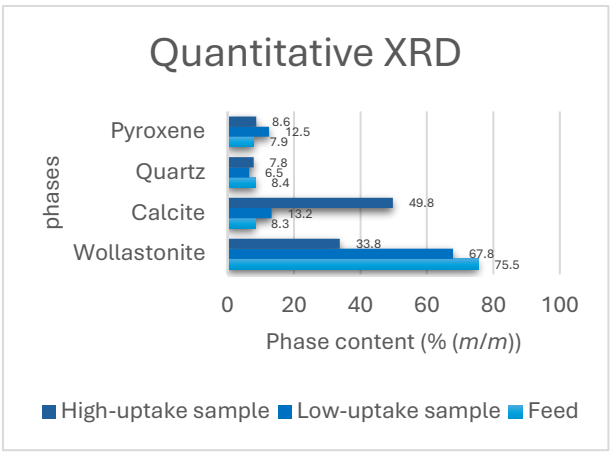

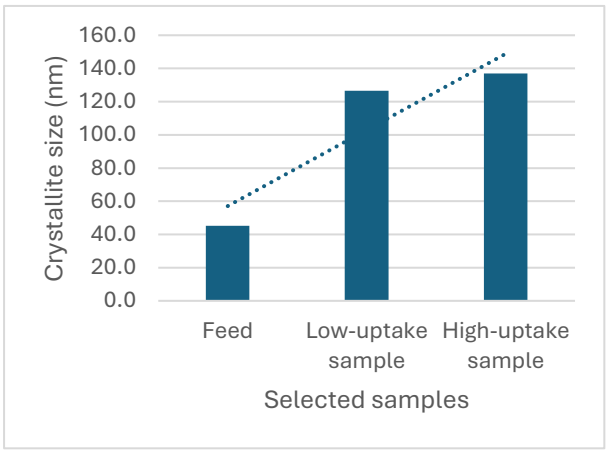

a

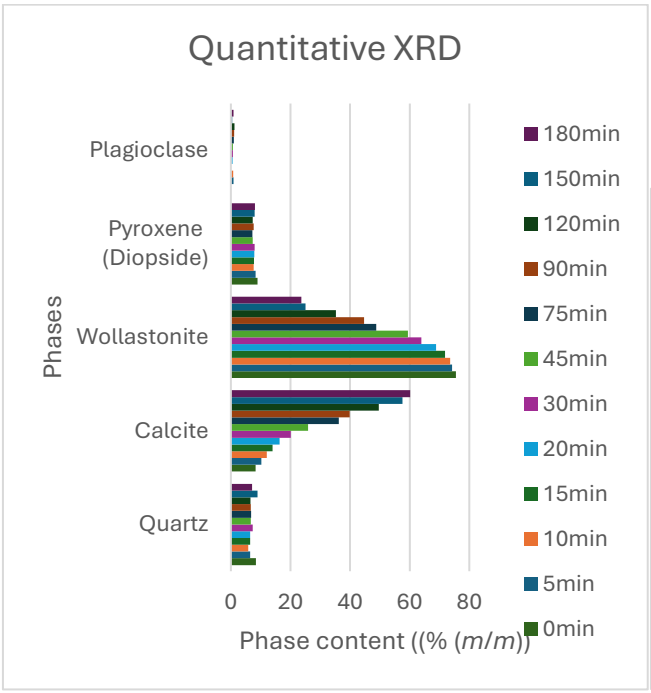

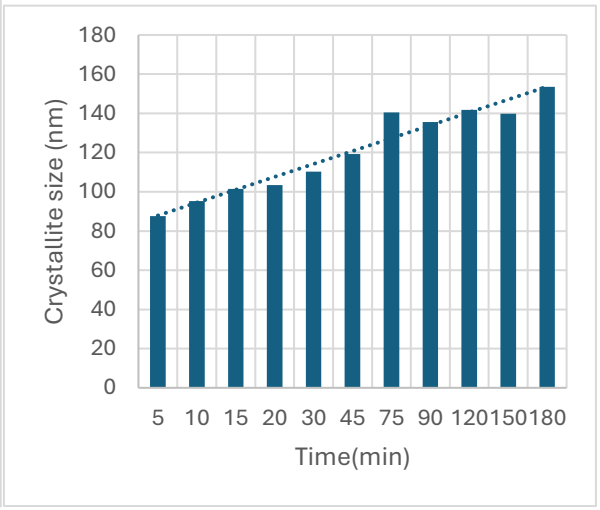

b

Figure 2 Obtained phases from a. each selected condition in comparison with the feed, and b. Carbonation duration (Kinetics study) and the trend in changes in their calcite crystallite size.

3.3 Morphological Changes Under Low and High Uptake Conditions

Scanning electron microscopy (SEM) images show carbonate particles on silicate grains exhibiting a rhombohedral morphology, which is consistent with calcite. Elemental mapping corroborates this

identification: calcium-rich domains align with the rhombohedral features, while silicon-rich regions correspond to the underlying wollastonite matrix [15,16,27]. In the feed sample (Figure 3.a), no rhombohedral carbonate crystals were detected despite targeted examination. The low-uptake product (Figure 3.b) displays scattered rhombohedral, forming a thin, discontinuous film. In contrast, the high-uptake product (Figure 3-C) contains abundant and locally coalesced rhombohedral particles, resulting in a denser product layer and partial bridging between grains. These findings indicate a larger areal coverage of calcite in the high-uptake sample compared to the low-uptake sample. In the EDX mapping, the displayed colors are software-assigned overlays, with red and green indicating the relative X-ray intensities of Ca and Si at each pixel, respectively. Areas enriched in Ca (high Ca/Si ratio) are attributed to $CaCO_3$ precipitates (calcite), while regions enriched in Si (low Ca/Si ratio) correspond to the silicate matrix (wollastonite/$CaSiO_3$). The map shows that Ca-rich, reddish crystals are distributed on and locally coat the Si-rich, greenish wollastonite grain, suggesting that calcite formed as a secondary precipitate on the wollastonite surface during carbonation. These observations are also reported in other studies under different conditions, such as high CO_2 partial pressure, additives, or accelerators [14,16,19]. Spectra acquired from representative points or areas in these regions demonstrate that elemental peak heights directly correspond to the map colors (c.f.Figure 3.b. The reddish crystals produce spectra dominated by Ca (and O) with relatively weak Si signals, whereas the greenish grain surface displays a stronger Si signal along with Ca and O, consistent with the underlying wollastonite or silicate phase.

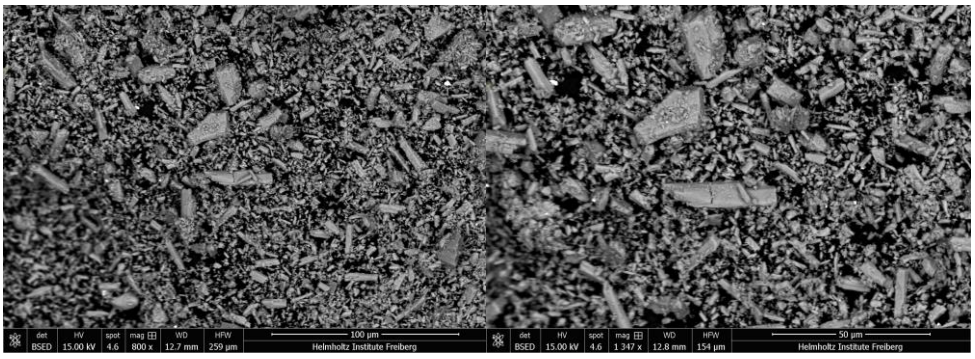

a.

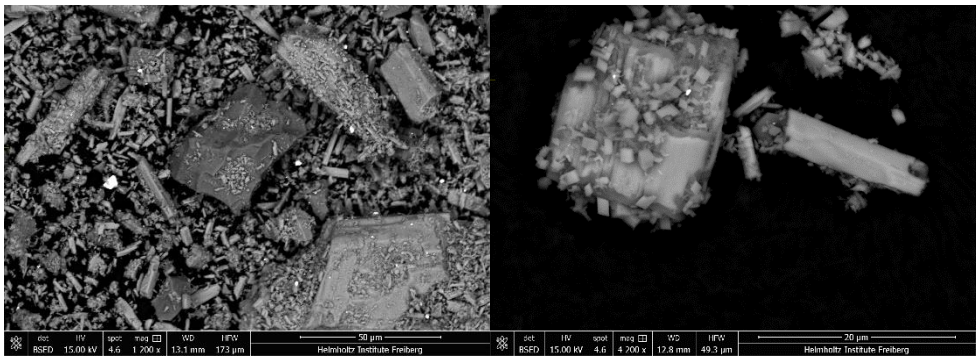

b.

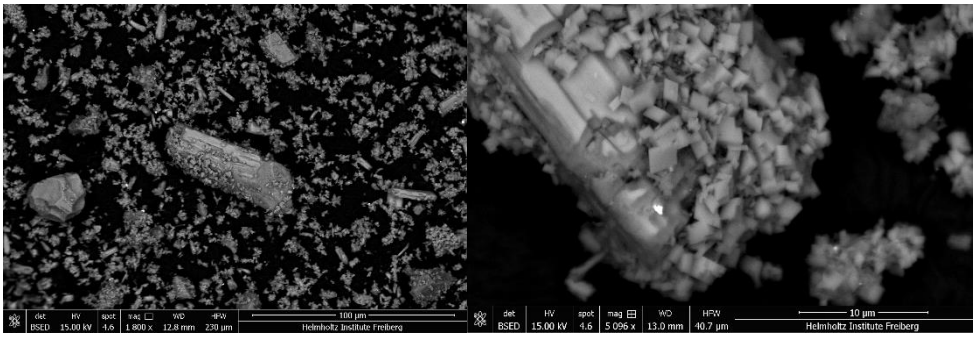

c.

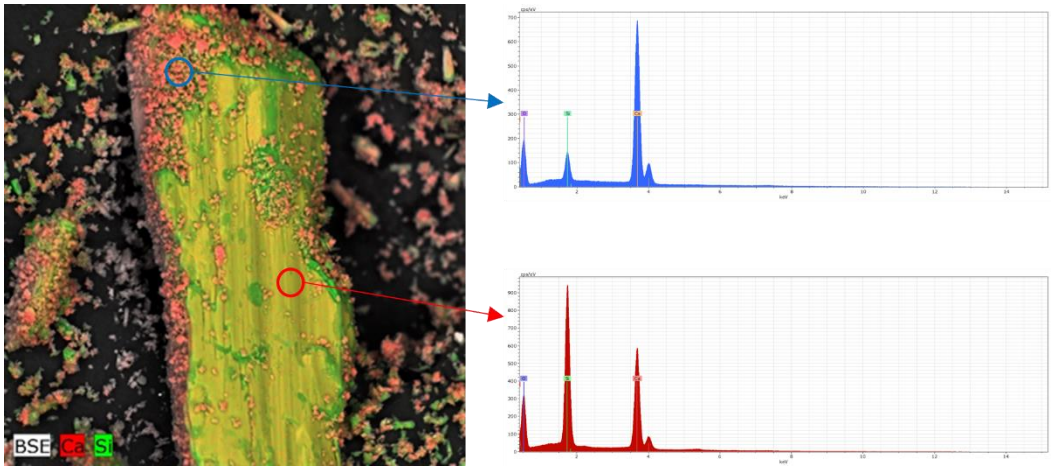

d.

Figure 3 SEM Images of a. the Feed, b. the lowest carbonated sample, and c. the highest carbonated sample. d. The elemental map from the rhombohedral calcite crystal structure (Upper spectra) and wollastonite (Lower spectra).

3.4 Microstructural Evolution, Surface Passivation, and the Role of Mass Transport

The distinct outcomes observed under high and low-uptake carbonation conditions underscore the importance of mixing efficiency, CO_2 availability, and the solid-to-liquid (S/L) ratio in controlling reaction kinetics and microstructural evolution during wollastonite carbonation. Both experiments used the same feed particle-size distribution; thus, differences between the resulting products are attributed to condition-dependent changes during carbonation rather than initial particle size. Notably, carbonation reduces the BET specific surface area (SSA) (Table 5) relative to the feed in both cases: the feed exhibits 4.67 $m^2.g^{-1}$, the low-uptake product decreases to 3.06 $m^2.g^{-1}$, and the high-uptake product reaches 4.29 $m^2.g^{-1}$. This reduction in SSA indicates that carbonation generally results in partial loss of accessible surface, consistent with product-layer coverage, pore-mouth occlusion, and/or particle agglomeration. In the high-uptake regime (900 rpm, 10 % S/L, 700 $mL.min^{-1}$ CO_2), vigorous mixing and high CO_2 supply promote efficient slurry circulation, frequent renewal of reactive surfaces, and sustained supersaturation with respect to $CaCO_3$. These conditions enhance the degree of carbonation and favor more distributed precipitation throughout the system. Although the SSA of the high-uptake product remains lower than that of the feed, it is relatively higher than the low-uptake product, indicating that favorable hydrodynamics mitigate passivation by limiting severe agglomeration and preserving a more open surface microstructure. Under these conditions, increased CO_2 availability and vigorous mixing maintain supersaturation and continuous surface renewal, which promote a high density of carbonate nuclei and a more uniform distribution of precipitates during the initial stages. As carbonation advances, the sustained supply of reactants facilitates ongoing crystal development and ripening, consistent with the larger apparent calcite crystallite size (see section3.2) observed in the highest-carbonated sample compared to the lowest-carbonated sample. Therefore, the high-uptake regime supports both extensive carbonate formation and the development of more mature calcite domains, while maintaining a higher accessible surface.

Conversely, the low-uptake condition (300 rpm, 30 % S/L, 100 $mL.min^{-1}$ CO_2) is characterized by a reduced mixing intensity and limited CO_2 transport, which lower supersaturation and slow the renewal of reactive surfaces. Under these conditions, carbonation is more likely to initiate at heterogeneous nucleation sites such as silicate edges, defects, or residual calcite. As a result, carbonate formation remains discontinuous and does not develop into a well-defined porous

product layer. This interpretation aligns with the XRD line-broadening results, which show a smaller apparent calcite crystallite size (See section3.2) in the lowest-carbonated sample compared to the highest-carbonated sample. These findings suggest limited crystal development or increased defect density when supersaturation and reactant supply are inadequate to support sustained growth.

Collectively, these findings indicate that the precipitation pathway and resulting product architecture, regulated by hydrodynamics, CO_2 supply, and S/L ratio, strongly influence accessible surface area and the degree of passivation during wollastonite carbonation. Favorable mass-transfer conditions promote distributed precipitation and a less blocked microstructure, while suboptimal conditions promote localized precipitation, agglomeration, and early surface blocking, resulting in a pronounced loss of accessible surface area.

These mechanistic interpretations, consistent with findings reported in the broader literature. [25], demonstrated that localized calcite precipitation can substantially alter pore geometry and reduce accessible reactivity, even at moderate reaction degrees. Additionally, [25,26] established that grain-coating and pore-filling precipitation modes have markedly different effects on permeability and porosity. In [26] It is also confirmed that supersaturation and CO_2 supply significantly influence carbonate precipitation pathways and resulting surface properties. These results demonstrate that optimizing hydrodynamic and mass-transport conditions are essential for preserving reactive surface exposure and reducing passivation during wollastonite carbonation leading to higher degrees of carbonation.

3.5 Density and Surface Area Changes Linked to Phase Replacement

The skeletal density of the raw wollastonite lies within the typical range for $CaSiO_3$ (2.86 $g.cm^{-3}$ – 3.09 $g.cm^{-3}$) [28], with the feed sample measured at 2.895 $g.cm^{-3}$ and a BET surface area of 4.67 $m^2.g^{-1}$. Under low-uptake conditions, the density remains nearly unchanged at 2.891 $g\ cm^{-3}$, whereas the BET surface area decreases substantially to 3.06 $m^2.g^{-1}$ (Table 5). This pairing of consistent density with reduced SSA indicates minimal phase replacement. This baseline establishes the threshold against which full carbonation effects are measured, highlighting its significance in understanding the progression of mineral transformation. In the high-uptake sample, the density decreases markedly to 2.719 $g.cm^{-3}$, consistent with partial replacement of wollastonite ($\approx$ 2.90 $g.cm^{-3}$) by lower-density calcite ($\approx$ 2.71 $g.cm^{-3}$) [29] and amorphous Si-rich phases

(≈ 2.1 g.cm^{-3} – 2.3 g.cm^{-3}). This confirms that carbonation progressed beyond surface coating and involved significant mineral transformation. The BET surface area also increases relative to the low-uptake product (4.29 m^2.g^{-1}) but remains lower than the feed. This intermediate SSA reflects the competing effects of (i) pore occlusion and surface smoothing that occurred earlier in the reaction, and (ii) the formation of a more porous carbonate–silica product coupled with mechanical surface renewal under higher shear. The increase in SSA might also be attributed to the nanoscale porosity formation within the amorphous silica networks, suggesting that these microstructural changes could be a pathway for future detailed microscopy-based exploration.

Table 5 Physical properties (SSA and Density) of selected carbonated sample and feed

	Sample Density g/cm^3	**BET Surface Area m^2/g**
Feed	2.895	4.67
Lowest	2.891	3.06
Highest	2.719	4.29

3.6 Thermal Decomposition Behavior of Carbonated Products (TGA/DTG)

Thermogravimetric analysis (TGA) of the two different carbonation regimes in uptake level, compared under an inert atmosphere (N_2) (Figure 4) shows that CO_2 release from carbonated calcium silicate systems typically occurs in the high-temperature decarbonation region (approximately 600°C - 800°C) [30–33], where $CaCO_3$ decomposes to CaO and CO_2. Mass loss observed below 200°C is generally assigned to the removal of physically adsorbed water and the dehydration of hydrated reaction products (e.g., Ca-modified silica gel), rather than carbonate decomposition [33]. In the carbonated silicate system, other kinds of calcium carbonate, metastable calcium carbonates, like aragonite and vaterite, could exist, as many studies show they might be decomposed in lower temperature regions, approximately 400°C – 600 °C [33–35] while the more stable or well-crystalline form of calcium carbonate, Calcite, decomposes at approximately 600°C - 800 °C. In these measurements, both the lowest- and highest-carbonated samples exhibit a distinct mass-loss step within this interval, confirming that the absorbed CO_2 is predominantly stored in carbonate, specifically calcite.

Although both DTG maxima occur within the calcite decarbonation region, the temperature of maximum CO_2 release differs: the lowest-carbonated sample peaks at 742.3°C, while the highest-carbonated sample peaks at 770.3°C. Such shifts for the same carbonate phase arise because the apparent decomposition temperature is sensitive to carbonate crystallinity, defect density, and microstructural confinement, as reported in previous studies regarding increasing crystallinity and carbonate "maturation" [33,36–38]. The earlier, lower-temperature DTG maximum in the lowest-carbonated sample aligns with limited carbonation, where carbonate is mainly present as sparse, thin, or defect-rich precipitates that decarbonate more readily. This interpretation is supported by XRD line-broadening, which indicates a smaller apparent calcite crystallite size in the lowest-carbonated sample, reflecting less-developed carbonate domains. In contrast, the highest-carbonated sample contains a larger carbonate fraction and a more developed assemblage, with a correspondingly larger apparent calcite crystallite size. This is consistent with more mature calcite domains or carbonate formed within a thicker carbonate-silica product layer, which can delay CO_2 release to higher temperatures.

DTG behavior is directly linked to the applied carbonation conditions (Table 1). Although both experiments were conducted at 90°C, the highest-uptake condition (900rpm, S/L = 10 %, 700 $mL \cdot min^{-1}$ CO_2) enhances gas-liquid mass transfer and surface renewal, sustaining supersaturation and enabling continued precipitation and carbonate development, as reflected by the higher DTG maximum (770.3 °C). In contrast, the lowest-uptake condition (300 rpm, S/L = 30 %, 100 $mL \cdot min^{-1}$ CO_2) restricts CO_2 availability and renewal of the mineral-fluid interface, leading to localized and discontinuous precipitation and less-developed carbonate that releases CO_2 at a lower DTG maximum (742.3 °C). Thus, the shift in CO_2-release temperature reflects not only on carbonate presence, but also on the influence of hydrodynamics and CO_2 supply on carbonate abundance, crystallite development, and the degree of confinement within the reaction products.

Regarding carbonation duration, the kinetics study shows a progressive increase in the DTG maximum temperature with increasing time (Figure 5), observed under the highest-uptake condition, indicating that the CO_2-bearing carbonate phase evolves during the reaction. This trend aligns with carbonate maturation, including increasing crystallinity and coherent domain size, possible transformation of less stable carbonate environments toward calcite, and greater confinement of carbonate within a growing carbonate-silica product layer. Collectively, these

effects enhance the apparent thermal stability of stored CO_2 and shift the maximum CO_2 release rate to higher temperatures as carbonation progresses.

In Figure 5 this difference in decomposition temperatures is more apparent when focusing on the longest and shortest carbonation times. The decomposition temperature for the shortest time is around 744.2°C, and for the longest time it is about 776°C. Figure 5

Figure 5 DTG-based evidence of time-dependent carbonate maturation during wollastonite carbonation. ***Left:*** *overlay of DTG curves measured under inert N_2 for all carbonation durations in the kinetics study, showing a systematic evolution of the main decarbonation reaction (calcite region).* ***Right:*** *extracted DTG maximum temperature (T_{max}, DTG)as a function of carbonation time, highlighting a progressive shift to higher temperature with increasing duration.*

shows this temperature for all the samples with different carbonation durations, which follow the same trend. Other works [26] also confirm that, with increasing reaction time, the formed calcite crystals are better defined and thermodynamically more stable, which is why they might decompose at higher temperatures. This trend also correlates with the calcite crystallite-size evolution discussed in section 3.2 As carbonation time increases, calcite crystals grow and become more mature, which can increase their apparent thermal stability and therefore shift the decomposition (maximum DTG) temperature to higher values. While wollastonite is representative, other silicates may exhibit distinct maturation kinetics.

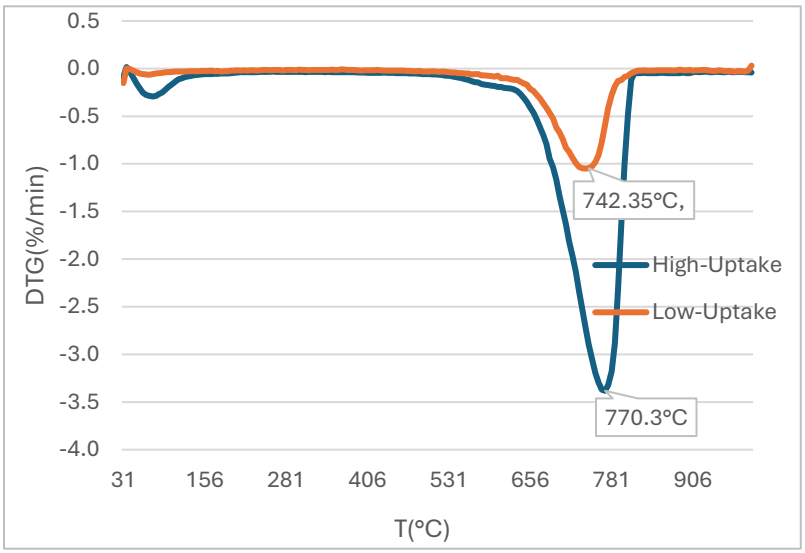

Figure 4 DTG curves of the two selected carbonated samples measured under N_2 (20 mL min^{-1}) from 30 to 1000 °C (20 K min^{-1}). The main decarbonation reaction occurs at ~650–850 °C, with DTG maxima at 742.3 °C (lowest uptake) and 770.3 °C (highest uptake)

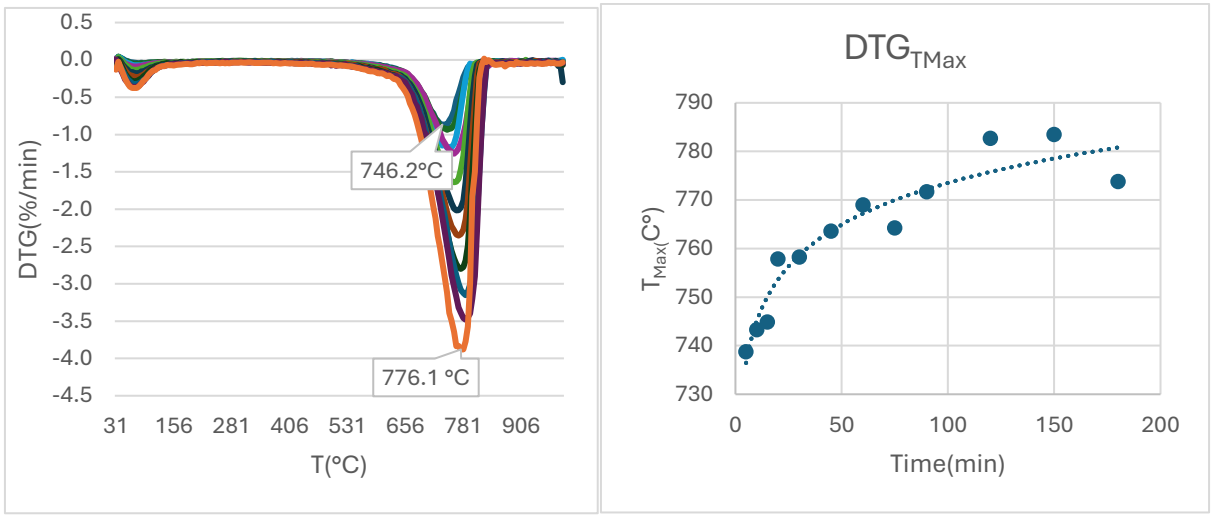

Figure 5 DTG-based evidence of time-dependent carbonate maturation during wollastonite carbonation. ***Left:*** *overlay of DTG curves measured under inert N_2 for all carbonation durations in the kinetics study, showing a systematic evolution of the main decarbonation reaction (calcite region).* ***Right:*** *extracted DTG maximum temperature (T_{max}, DTG)as a function of carbonation time, highlighting a progressive shift to higher temperature with increasing duration.*

3.7 Kinetics Model Fitting

Wollastonite was selected for the kinetics study of wet carbonation under near-ambient conditions due to its higher reactivity compared to other common minerals. This increased reactivity may result from differences in silica gel formation behavior or from its specific chemical composition relative to magnesium silicate (Mg-Si) minerals [1,11]. Specifically for this study, the high uptake carbonated wollastonite sample was chosen, as mentioned in section 2.2.3.

The experimental conversion data were evaluated using three kinetic models: the shrinking-core model ($SCM_{surface\ reaction}$) with chemical surface-reaction control, the SCM with diffusion control through a product layer ($SCM_{diffusion}$)[39,40] and the Avrami (Johnson-Mehl-Avrami-Kolmogorov JMAK) model [40,41].

According to the shrinking-core model (SCM), when the process is governed by a chemical reaction at the particle surface or by diffusion through the product layer, the corresponding kinetic expressions are provided by Eqs. (8) and (9), respectively.

$$1 - (1 - X)^{1/3} = k_s \cdot t \quad (8)$$

$$1 - 3(1 - X)^{2/3} + 2(1 - X) = k_d \cdot t \quad (9)$$

where k_s and k_d are the apparent rate constants for the chemical surface reaction-controlled and diffusion-controlled mechanisms, respectively; X is the CO_2uptake; and t is the reaction time.

The Avrami model, which is widely used to describe time-dependent transformation processes involving nucleation and growth, relates the extent of reaction to time according to:

$$X = 1 - e^{(-kAt^n)} \quad (10)$$

The linear form of the Avrami equation can be expressed as:

$$\ln[-\ln(1-X)] = \ln k_A + n\ln t \quad (11)$$

where k_A is the reaction rate constant, and n is the Avrami exponent, which indicates the nature of the transformation process.

summarizes the fitted parameters and goodness-of-fit metrics. Based on the R^2 values, the Avrami model and the SCM–surface reaction model provide the best overall description of the data, indicating that carbonation is governed primarily by surface-related processes over most of the reaction progress. The Avrami exponent determined in this study (n=0.9955) is a strong indicator of a first-order kinetic process. In solid-state kinetics, ($n \sim 1$) typically corresponds to an interface-controlled mechanism or to one-dimensional growth, which aligns well with the superior fit of the SCM–surface reaction model. In contrast, the $SCM_{diffusion}$ (Figure 6-C) model only matches the data at later conversion, suggesting that diffusion through a developing product layer becomes influential only at advanced stages rather than controlling the reaction from the beginning (Figure 6).

Table 6 Kinetic dataset for carbonation: measured CO_2 uptake (%), calculated conversion (-), and corresponding Avrami and SCM linearization terms used for model fitting (surface-reaction vs diffusion control).

Time (min)	**CO_2 uptake (%)**	**Conversion (-)**	**Avrami $\ln[-\ln(1-X)]=\ln k_A+n\ln t$**	**$SCM_{surface\ reaction}$ $1-(1-X)^{1/3} = k_s \cdot t$**	**$SCM_{diffision}$ $1-3(1-X)^{2/3}+2(1-X) = k_d \cdot t$**
0	0.00	0.00	-	0.00	0.00
5	1.02	0.04	-3.43	0.01	0.00
10	1.45	0.06	-3.06	0.01	0.00
15	2.56	0.09	-2.48	0.03	0.00
20	3.24	0.11	-2.23	0.03	0.00

30	4.94	0.17	-1.78	0.05	0.01
45	7.20	0.24	-1.36	0.08	0.02
60	9.58	0.32	-1.03	0.11	0.04
75	11.01	0.36	-0.86	0.13	0.05
90	12.38	0.40	-0.71	0.15	0.06
120	15.63	0.51	-0.39	0.20	0.11
150	17.82	0.58	-0.20	0.24	0.14
180	19.68	0.64	-0.04	0.27	0.19
Theory	31.8	1.00	-	1.00	1.00

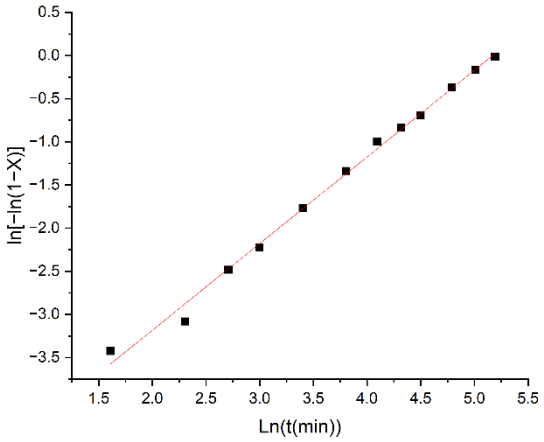

Avrami	
Intercept (lnKa)	-5.16314 ± 0.08231
Slope (n)	0.99293 ± 0.0212
Residual Sum of Squares	0.06383
Pearson's r	0.99773
R-Square (COD)	0.99546
Adj. R-Square	0.99501

a. Avrami

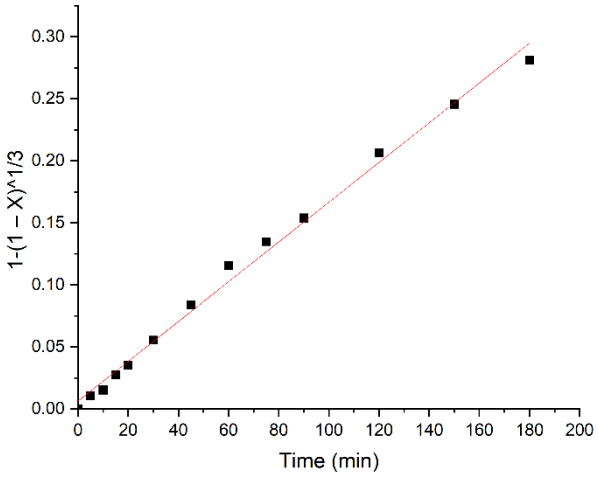

SCM (Surface)	
Intercept	0.0065 ± 0.00318
Slope (K_s)	0.00156 ± 3.81057E-5
Residual Sum of Squares	6.55977E-4
Pearson's r	0.99674
R-Square (COD)	0.99348
Adj. R-Square	0.99289

b. Shrinking Core (Surface reaction)

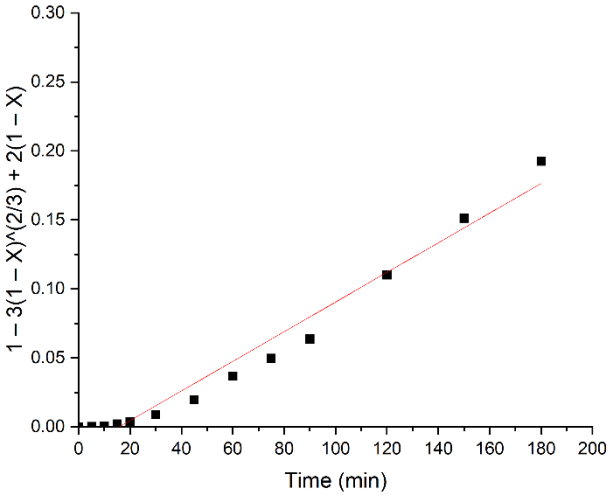

SCM (Diffision)	
Intercept	-0.01617 ± 0.00464
Slope (K_d)	0.00103 ± 5.56758E-5
Residual Sum of Squares	0.0014
Pearson's r	0.98437
R-Square (COD)	0.96898
Adj. R-Square	0.96616

c. Shrinking Core (Diffusion)

Figure 6 Linearized model fits: (a) Avrami (JMAK), (b) SCM surface-reaction control, (c) SCM product-layer diffusion. Avrami and SCM-surface act as surface-controlled representatives for growth and interface reaction, respectively; SCM-diffusion shows good linearity only late, consistent with product-layer transport emerging after substantial conversion.

Collectively, the model fits support a multi-stage reaction mechanism. The $SCM_{surface\ reaction}$ model characterizes the early-to-intermediate regime, which is consistent with an interface-controlled step where wollastonite dissolution supplies Ca^{2+} to the reactive boundary layer. The Avrami model describes the subsequent precipitation regime, during which $CaCO_3$ forms through nucleation and growth. The convergence of the Avrami exponent ($n \sim 1$) with the SCM-surface model confirms that the rate-limiting step is predominantly the chemical reaction at the phase boundary. At longer reaction times, the enhanced performance of the $SCM_{diffusion}$ model aligns with rising transport resistance due to the developing carbonate-silica product layer, resulting in a diffusion-driven tail while still maintaining the dominant surface-controlled behavior.

Independent structural and thermal analyses support this kinetic sequence. Time-resolved QXRD data reveal a progressive increase in calcite content and a corresponding decrease in wollastonite, consistent with a dissolution-precipitation mechanism. Additionally, the apparent calcite crystallite size increases with carbonation duration, indicating ongoing carbonate development during the Avrami-governed stage. SEM/EDX analyses further confirm precipitation on a wollastonite-derived substrate, with Ca-rich rhombohedral domains forming as carbonation advances. In line with microstructural evolution, the DTG maximum temperature (Figure 5) shifts to higher values for more strongly carbonated products produced after a longer reaction time (i.e. 180 min). (e.g. 744.3°C for the lowest-carbonated sample after 5 min compared to 776.1°C for the highest-carbonated sample with the longest carbonation duration), indicating a more developed and thermally stable carbonate assemblage at higher conversion, which takes longer. Surface-property measurements also support the model-based interpretation: under favorable mass-transfer conditions, the specific surface area (SSA) remains relatively high, while under less favorable conditions, a greater decrease in SSA is consistent with earlier surface masking and pore-mouth occlusion, which promote diffusion limitations at later stages.

These findings align with previous mechanistic studies. For instance, Daval et al. [12,16] demonstrated that under static or weakly mixed conditions, wollastonite carbonation remains controlled by interfacial processes, and carbonate precipitation does not necessarily fill the fractured or porous silica-rich layer. This supports an initially interface-dominated regime before

transport limitations become significant in certain microstructural contexts. In summary, the combined kinetic modeling and multi-technique characterization indicate that wollastonite wet carbonation proceeds through an initial interface-controlled dissolution step, followed by a nucleation and growth-dominated precipitation regime, and concludes with a late-stage diffusion-influenced phase as the product layer develops.

4 Conclusion and Outlook

We demonstrated that operating conditions affect not only the degree of wollastonite carbonation but also the resulting product texture and CO_2-storage characteristics. The samples analyzed in this study were selected from a systematic screening phase of additive-free, near-ambient wet carbonation, representing distinct carbonation outcomes. Multiple complementary characterization techniques were employed to develop a mechanistic interpretation of carbonation under these conditions. Specifically, XRD was used to monitor mineralogical evolution and carbonate crystallinity; SEM/EDX to resolve product-layer morphology and spatial elemental distributions; BET and skeletal density to quantify changes in accessible surface area and bulk transformation; and TGA/DTG to assess CO_2 release behavior and the apparent thermal stability of the carbonated phases.

The combined evidence supports a dissolution–precipitation pathway, wherein Ca^{2+} release from wollastonite is followed by $CaCO_3$ nucleation and growth. The precipitation mode is strongly influenced by hydrodynamics and mass transport. Q XRD confirms progressive conversion of wollastonite into calcite under favorable conditions, while other silicate phases remain largely unchanged. Line-broadening analysis reveals an increase in apparent calcite crystallite size with increasing conversion and reaction progress, consistent with carbonate maturation as carbonation proceeds, as indicated by comparative crystallite sizes obtained using a consistent fitting protocol. SEM/EDX observations corroborate these findings: low-uptake conditions result in sparse, discontinuous Ca-rich rhombohedral precipitates on largely intact silicate grains, whereas high-uptake conditions produce abundant, coalescing carbonate domains that more extensively cover and bridge particles, reflecting a more developed carbonate–silica product texture. Changes in BET surface area and skeletal density capture the corresponding microstructural transition from early surface masking and limited replacement to substantial mineral transformation. These trends align

with the observed shift in DTG_T_{max} to higher temperatures for more strongly carbonated products, indicating a more stable and developed carbonate assemblage.

The time-resolved kinetic study further substantiates this mechanistic framework. As carbonation duration increases, calcite content rises while wollastonite content declines, and carbonate crystallite size increases, indicating ongoing precipitation and growth throughout the reaction. The kinetic data are best described by an Avrami-type nucleation–growth model, which is consistent with an initial surface or interface-controlled stage, followed by a growth regime and a subsequent diffusion-influenced phase. This interpretation aligns with the observed microstructural and phase-evolution trends. Collectively, these results establish a coherent mechanistic basis for optimizing wollastonite carbonation by adjusting hydrodynamics and mass-transport conditions to maximize conversion and control product morphology and CO_2 storage stability.

Future work should (i) quantify amorphous Si-rich products and resolve the carbonate–silica layer architecture in more detail (e.g., internal-standard XRD/Rietveld and cross-sectional microscopy), (ii) verify pore-network evolution and pore-mouth occlusion with pore-size distribution measurements, and (iii) refine crystallite size/strain estimates using instrument-corrected line-broadening approaches.

Acknowledgements

This work is part of the CO_2Valorize project, which has received funding from the European Union's Horizon Europe research and innovation programme under the Marie Skłodowska-Curie Grant Agreement No. 101073547. The authors would like to thank Dr. Bradley Martin Guy and Ava Holowenko for assistance with SEM-EDX measurements at HZDR, Helmholtz Institute Freiberg for Resource Technology (HIF); and Erik Löwer from TU Bergakademie Freiberg for assistance with BET and pycnometer analyses.

Data availability

The experimental data which this work is based upon is to be found in a data repository by Homaee et al.

References

[1] A. Sanna, M. Uibu, G. Caramanna, R. Kuusik, M.M. Maroto-Valer, A review of mineral carbonation technologies to sequester CO_2, Chem. Soc. Rev. 43 (2014) 8049–8080. https://doi.org/10.1039/C4CS00035H.

[2] S.J. Davis, N.S. Lewis, M. Shaner, S. Aggarwal, D. Arent, I.L. Azevedo, S.M. Benson, T. Bradley, J. Brouwer, Y.-M. Chiang, C.T.M. Clack, A. Cohen, S. Doig, J. Edmonds, P. Fennell, C.B. Field, B. Hannegan, B.-M. Hodge, M.I. Hoffert, E. Ingersoll, P. Jaramillo, K.S. Lackner, K.J. Mach, M. Mastrandrea, J. Ogden, P.F. Peterson, D.L. Sanchez, D. Sperling, J. Stagner, J.E. Trancik, C.-J. Yang, K. Caldeira, Net-zero emissions energy systems, Science 360 (2018) eaas9793. https://doi.org/10.1126/science.aas9793.

[3] A. Sanna, M. Dri, M.R. Hall, M. Maroto-Valer, Waste materials for carbon capture and storage by mineralisation (CCSM) – A UK perspective, Applied Energy 99 (2012) 545–554. https://doi.org/10.1016/j.apenergy.2012.06.049.

[4] E.R. Bobicki, Q. Liu, Z. Xu, Mineral carbon storage in pre-treated ultramafic ores, Minerals Engineering 70 (2015) 43–54. https://doi.org/10.1016/j.mineng.2014.08.009.

[5] A. Ismailov, N. Merilaita, E. Levänen, Accelerated Carbonation of High-Calcite Wollastonite Tailings, Minerals 14 (2024) 415. https://doi.org/10.3390/min14040415.

[6] H. Ostovari, L. Müller, J. Skocek, A. Bardow, From Unavoidable CO_2 Source to CO_2 Sink? A Cement Industry Based on CO_2 Mineralization, Environ. Sci. Technol. 55 (2021) 5212–5223. https://doi.org/10.1021/acs.est.0c07599.

[7] A. Bărbulescu, K. Hosen, Cement Industry Pollution and Its Impact on the Environment and Population Health: A Review, Toxics 13 (2025) 587. https://doi.org/10.3390/toxics13070587.

[8] M. Hanifa, R. Agarwal, U. Sharma, P.C. Thapliyal, L.P. Singh, A review on CO2 capture and sequestration in the construction industry: Emerging approaches and commercialised technologies, Journal of CO2 Utilization 67 (2023) 102292. https://doi.org/10.1016/j.jcou.2022.102292.

[9] A. Ahmed, Z.F. Abu Hassan, Critical review of methods, mechanisms, and feedstocks in mineral carbonation for enhanced carbon neutrality: From waste to climate solution, Science of The Total Environment 980 (2025) 179544. https://doi.org/10.1016/j.scitotenv.2025.179544.

[10] M.A. Saleh, M.P. Ryan, J.P.M. Trusler, S. Krevor, The interfacial processes controlling carbon dioxide mineralisation in magnesium and calcium silicates, Fuel 380 (2025) 132969. https://doi.org/10.1016/j.fuel.2024.132969.

[11] S.J. Gerdemann, W.K. O'Connor, D.C. Dahlin, L.R. Penner, H. Rush, Ex Situ Aqueous Mineral Carbonation, Environ. Sci. Technol. 41 (2007) 2587–2593. https://doi.org/10.1021/es0619253.

[12] D. Daval, I. Martinez, J. Corvisier, N. Findling, B. Goffé, F. Guyot, Carbonation of Ca-bearing silicates, the case of wollastonite: Experimental investigations and kinetic modeling, Chemical Geology 265 (2009) 63–78. https://doi.org/10.1016/j.chemgeo.2009.01.022.

[13] J. Back, R. Zevenhoven, J. Fagerlund, P. Sorjonen-Ward, Mineral Carbonation Using Mine Tailings - a Strategic Overview of Potential and Opportunities, SSRN Journal (2022). https://doi.org/10.2139/ssrn.4285256.

[14] F. Di Lorenzo, C. Ruiz-Agudo, A. Ibañez-Velasco, R. Gil-San Millán, J. Navarro, E. Ruiz-Agudo, C. Rodriguez-Navarro, The Carbonation of Wollastonite: A Model Reaction to Test Natural and Biomimetic Catalysts for Enhanced CO2 Sequestration, Minerals 8 (2018) 209. https://doi.org/10.3390/min8050209.
[15] W.J.J. Huijgen, G.-J. Witkamp, R.N.J. Comans, Mechanisms of aqueous wollastonite carbonation as a possible CO2 sequestration process, Chemical Engineering Science 61 (2006) 4242–4251. https://doi.org/10.1016/j.ces.2006.01.048.
[16] D. Daval, I. Martinez, J.-M. Guigner, R. Hellmann, J. Corvisier, N. Findling, C. Dominici, B. Goffe, F. Guyot, Mechanism of wollastonite carbonation deduced from micro- to nanometer length scale observations, American Mineralogist 94 (2009) 1707–1726. https://doi.org/10.2138/am.2009.3294.
[17] L. Monasterio-Guillot, F. Di Lorenzo, E. Ruiz-Agudo, C. Rodriguez-Navarro, Reaction of pseudowollastonite with carbonate-bearing fluids: Implications for CO2 mineral sequestration, Chemical Geology 524 (2019) 158–173. https://doi.org/10.1016/j.chemgeo.2019.06.011.
[18] K. Svensson, A. Neumann, F. Feitosa Menezes, C. Lempp, H. Pöllmann, Carbonation of Natural Wollastonite at Non-Ambient Conditions Relevant for CCS—the Possible Use as Cementitious Material in Wellbores, Applied Sciences 9 (2019) 1259. https://doi.org/10.3390/app9061259.
[19] M.Z. Kashim, H. Tsegab, O. Rahmani, Z.A. Abu Bakar, S.M. Aminpour, Reaction Mechanism of Wollastonite In Situ Mineral Carbonation for CO_2 Sequestration: Effects of Saline Conditions, Temperature, and Pressure, ACS Omega 5 (2020) 28942–28954. https://doi.org/10.1021/acsomega.0c02358.
[20] C.Y. Tai, W. -R. Chen, S. Shih, Factors affecting wollastonite carbonation under CO_2 supercritical conditions, AIChE Journal 52 (2006) 292–299. https://doi.org/10.1002/aic.10572.
[21] M. Ghoorah, B.Z. Dlugogorski, R.D. Balucan, E.M. Kennedy, Selection of acid for weak acid processing of wollastonite for mineralisation of CO2, Fuel 122 (2014) 277–286. https://doi.org/10.1016/j.fuel.2014.01.015.
[22] Y. Min, Q. Li, M. Voltolini, T. Kneafsey, Y.-S. Jun, Wollastonite Carbonation in Water-Bearing Supercritical CO_2 : Effects of Particle Size, Environ. Sci. Technol. 51 (2017) 13044–13053. https://doi.org/10.1021/acs.est.7b04475.
[23] N. Doebelin, R. Kleeberg, *Profex* : a graphical user interface for the Rietveld refinement program *BGMN*, J Appl Crystallogr 48 (2015) 1573–1580. https://doi.org/10.1107/S1600576715014685.
[24] Z. Tabrizi, C. Rodriguez, E. Barbera, W.R. Leal Da Silva, F. Bezzo, Wet Carbonation of Industrial Recycled Concrete Fines: Experimental Study and Reaction Kinetic Modeling, Ind. Eng. Chem. Res. 64 (2025) 21412–21425. https://doi.org/10.1021/acs.iecr.5c02835.
[25] Y. Zhang, H. Yang, Q. Zhang, Q. Qian, C. Zhang, K. Wu, P. Shen, Microstructural Evolution of Calcium Sulfoaluminate Cement during the Wet-Carbonation Process, Buildings 14 (2024) 343. https://doi.org/10.3390/buildings14020343.
[26] Y. Mao, P. He, S. Drissi, J. Zhang, X. Hu, C. Shi, Effect of conditions on wet carbonation products of recycled cement paste powder, Cement and Concrete Composites 144 (2023) 105307. https://doi.org/10.1016/j.cemconcomp.2023.105307.
[27] W. Ashraf, J. Olek, N. Tian, Multiscale characterization of carbonated wollastonite paste and application of homogenization schemes to predict its effective elastic modulus, Cement

and Concrete Composites 72 (2016) 284–298. https://doi.org/10.1016/j.cemconcomp.2016.05.023.
[28] A. Nichols, M.C J.W., Handbook of Mineralogy, n.d.
[29] Introduction to Mineralogy and Petrology, ScienceDirect (n.d.). http://www.sciencedirect.com:5070/book/monograph/9780128205853/introduction-to-mineralogy-and-petrology (accessed January 4, 2026).
[30] R. Igami, G. Igarashi, A. Aili, D. Minato, R. Kurihara, I. Maruyama, Clinker mineral formation and thermal decomposition of calcium carbonates in carbonated tobermorites: Mechanism of CO2 release in low-temperature ranges, Cement and Concrete Research 197 (2025) 107969. https://doi.org/10.1016/j.cemconres.2025.107969.
[31] K. Scrivener, R. Snellings, B. Lothenbach, eds., A Practical Guide to Microstructural Analysis of Cementitious Materials, 0 ed., CRC Press, 2018. https://doi.org/10.1201/b19074.
[32] S. Tsivilis, G. Kakali, E. Chaniotakis, A. Souvaridou, A Study on the Hydration of Portland Limestone Cement by Means of TG, Journal of Thermal Analysis and Calorimetry 52 (1998) 863–870. https://doi.org/10.1023/A:1010139312958.
[33] Y. Mu, Z. Liu, F. Wang, Comparative Study on the Carbonation-Activated Calcium Silicates as Sustainable Binders: Reactivity, Mechanical Performance, and Microstructure, ACS Sustainable Chem. Eng. 7 (2019) 7058–7070. https://doi.org/10.1021/acssuschemeng.8b06841.
[34] F. Kaddah, E. Roziere, H. Ranaivomanana, O. Amiri, Complementary use of thermogravimetric analysis and oven to assess the composition and bound CO2 content of recycled concrete aggregates, Developments in the Built Environment 15 (2023) 100184. https://doi.org/10.1016/j.dibe.2023.100184.
[35] M. Maciejewski, H.-R. Oswald, A. Reller, Thermal transformations of vaterite and calcite, Thermochimica Acta 234 (1994) 315–328. https://doi.org/10.1016/0040-6031(94)85155-7.
[36] P. Allah, H. Nguyen, M. Illikainen, P. Kinnunen, P. Perumal, Wet carbonation of wollastonite with pH-modified solutions at ambient conditions: Insights from a geochemical model, Journal of CO2 Utilization 101 (2025) 103194. https://doi.org/10.1016/j.jcou.2025.103194.
[37] W. Ashraf, J. Olek, Elucidating the accelerated carbonation products of calcium silicates using multi-technique approach, Journal of CO2 Utilization 23 (2018) 61–74. https://doi.org/10.1016/j.jcou.2017.11.003.
[38] W. Ashraf, J. Olek, Carbonation activated binders from pure calcium silicates: Reaction kinetics and performance controlling factors, Cement and Concrete Composites 93 (2018) 85–98. https://doi.org/10.1016/j.cemconcomp.2018.07.004.
[39] M. Tu, H. Zhao, Z. Lei, L. Wang, D. Chen, H. Yu, T. Qi, Aqueous Carbonation of Steel Slag: A Kinetics Study, ISIJ International 55 (2015) 2509–2514. https://doi.org/10.2355/isijinternational.ISIJINT-2015-142.
[40] E. N. Yeremin, The Foundations Of Chemical Kinetics Mir, Mir Publishers, 1979. http://archive.org/details/e.-n.-yeremin-the-foundations-of-chemical-kinetics-mir-1979 (accessed January 19, 2026).
[41] A.K. Jena, M.C. Chaturvedi, Phase Transformation in Materials, Prentice Hall, 1992.